Fluorescence Microscopy Imaging of Light-Harvesting in Self-Assembled Nanofibers of Naphthalenediimides towards Perylenediimide Guests

Ramarani Sethy,[†,‡] Arnaud Brosseau,[‡] Takuya Nakashima, [†,§] Tsuyoshi Kawai,[,†] Rémi Métivier[*,‡]*

[†]Division of Material Science, Graduate School of Science and Technology, Nara Institute of Science and Technology (NAIST), Ikoma, Nara 630-0192, Japan.

[‡]Université Paris-Saclay, ENS Paris-Saclay, CNRS, PPSM, 91190 Gif-sur-Yvette, France.

[§]Department of Chemistry, Graduate School of Science, Osaka Metropolitan University, Sumiyoshi-ku, Osaka 558-8585, Japan.

KEYWORDS. Light-harvesting, excitation energy transfer, fluorescence microscopy imaging, atomic force microscopy, polarization, self-assembly

ABSTRACT. The self-assembly of a bichromophoric naphthalenediimide (NDI) into nanofibers showed efficient energy transfer (light-harvesting) to perylenediimide (PDI) molecules through host-guest interaction, which can be visualized by microscopy using samples deposited on glass surfaces. In combination with atomic force microscopy (AFM), spectral and polarization analyses,

fluorescence imaging unveiled the inhomogeneity, packing defects, and relative spatial arrangement of PDI and NDI molecular units, which were found to affect the exciton mobility along the NDI nanofibers and the energy transfer efficiency from NDI to PDI guests. Fluorescence micro-spectroscopy shows that efficient energy transfer occurs from NDI nanofibers to isolated PDI molecules and their partial self-aggregates. The NDI nanofibers emit strong blue polarized emission, while the emission corresponding to PDI guest molecules is weakly polarized, indicating the local disruption of NDI chromophores-ordering upon PDI guest binding.

MAIN TEXT

1. Introduction

Directed excitation energy transport at the nanoscale in supramolecular assemblies is of great importance for the development of new organic optoelectronic devices and next-generation solar cells.[1–4] It is well known that the highly symmetric arrangement of the chlorophyll pigments in the natural light-harvesting systems promotes efficient directional excitation energy flow to the reaction center.[5–9] This highly directed energy transport in such natural light-harvesting systems has been a great inspiration for their artificial counterparts, nano-antenna systems. For instance, organic dyes, polymer conjugates, organic crystalline films, and various types of inorganic nanoparticles are among the best candidates due to their high exciton mobility at the nanoscale level.[9–25] However, the precise control of chromophore spacing and organization, taking into account the inhomogeneity and defects of such nanomaterials during self-assembly preparation, remains a challenge for these artificial light-harvesting systems.[26,27] A comprehensive understanding and characterization of the structural insight and energy transfer dynamics of such molecular assemblies is required to control/alter their functionality for the development of new optoelectronic devices.[1,28] For their practical application, it is also necessary to immobilize these nanostructures on solid substrates without destroying their supramolecular structures, optical and photophysical properties. Recently, precise fluorescence microscopy imaging has been implemented as a novel technique in various nanostructured materials for *in situ* and real time visualization of their dynamic behavior,[29–32] visual characterization of defects in metallic organic 3D frameworks and liquid crystals,[33–35] inhomogeneity in inorganic hybrid crystalline nanostructures,[36,37] conformational analysis and molecular weight determination of polymers[38,39] and characterization of polymerization progress[40] and micro-dispersion in organic-inorganic

composites.[41,42] Therefore, microscopy imaging can be used as a simple tool to understand and visualize the light-harvesting phenomena of supramolecular nanostructures probed by energy transfer.[43] Polarization experiments,[28] localizing both position and orientation of the chromophore units that are present in such assemblies, can well characterize the influence of the anisotropic shape/structure[44,45] of the supramolecular assembly on its light-harvesting property. We have reported the supramolecular assembly of a chiral bichromophoric naphthalenediimide (molecule (*R*)-**1**NDI in Scheme **1**, left) into nanofibers, which showed absolute enantioselective recognition of a chiral perylenediimide bichromophoric derivative (molecule (*S*)-**2**PDI in Scheme **1**, right) with opposite handedness by host-guest interaction in methylcyclohexane (MCH) rich solution.[46] This chiral recognition of nanofibers towards the (*S*)-**2**PDI guest molecule was evaluated by Förster resonance energy transfer (FRET),where the fast and efficient exciton migration among the (*R*)-**1**NDI chromophore units along the nanofibers efficiently transport the excitation energy to the bound (*S*)-**2**PDI guest molecules.[47] The chiral arrangement of the right-handed (*R*)-**1**NDI molecular units is driven by the chiral cyclohexane-1,2-diamine moiety via hydrogen bonding, and the bulky ethoxy substituents at (*R*)-**1**NDI core disfavor strong intermolecular π– π interaction in the (*R*)-**1**NDI assembly, resulting in semi-open π–space chiral binding motifs that enable highly selective recognition of (*S*)-**2**PDI guests via π–surface interaction.[46–48] In this work, we further investigate possible excitonic delocalization along (*R*)-**1**NDI nanofibers on a glass substrate and demonstrate efficient light-harvesting properties towards (*S*)-**2**PDI guest molecules. Extensive analysis of their spectral properties, along with significant energy transfer efficiency on individual nanofibers and their anisotropic local environments, is demonstrated using precise wide-field fluorescence microscopy imaging with polarization analysis in combination with atomic force microscopy (AFM).

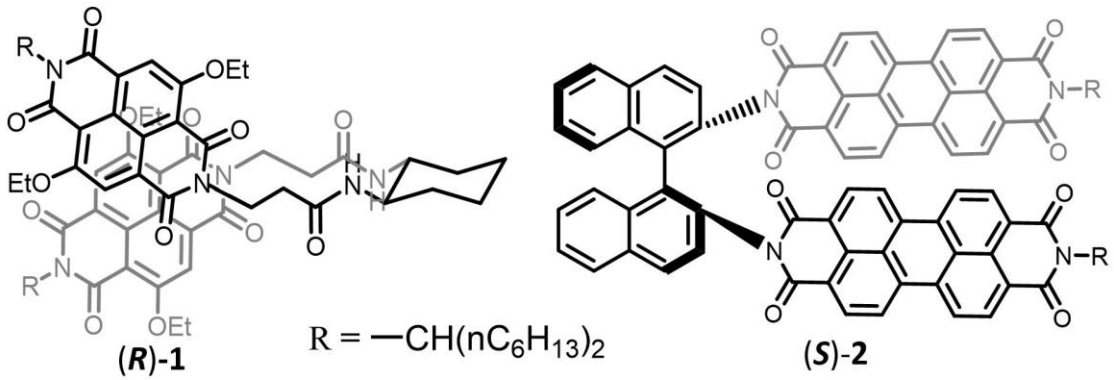

Scheme **1**. Molecular structure of *R*-isomer of **1** (full name: (*R*)-**1**NDI) and *S*-isomer of **2** (full name: (*S*)-**2**PDI) respectively.

2. Materials and Methods

Sample Preparation

(*R*)-**1**NDI and (*S*)-**2**PDI were prepared according to synthetic procedures as described in our previous literature.[46–48] Coassemblies of (*R*)-**1**NDI (1.0×10^{-5} M) and (*S*)-**2**PDI (1.5×10^{-7} M) were prepared in a mixture of chloroform/MCH (1:19) with annealing at 95°C followed by cooling to room temperature and then drop cast onto alkyl-treated and untreated glass slides.[49,50] We modified the glass slides with alkylsilanes to make the glass surface hydrophobic and compatible with the supramolecular complex. Prior to silanization, the substrates were thoroughly cleaned as follows: the glass slides were rinsed 2-3 times with acetone, then sonicated in an ultrasonic bath for 20 minutes in 50% methanol/water, followed by an additional 20 minutes in chloroform, and further allowed to air dry. The dried glass slides were treated with plasma cleaner for 60 seconds as a surface activation method. After plasma cleaning, the glass slides were kept in an oven for 1 hour at 110 °C to produce a dehydrated surface. They were then immersed in 2 vol% alkylsilane

solutions (n-octyltriethoxysilane and n-dodecyltriethoxysilane) in toluene and dried in an oven at 110 °C under N_2 atmosphere for 1 hour to remove toluene completely before microscopy imaging. The blank slides were subjected to AFM imaging to examine the homogeneity of the surface. AFM images (10 × 10 μm) of both alkylsilane-substituted glass slides (n-octyltriethoxysilane and n-dodecyltriethoxysilane) showed uniform surface roughness with low values (Figure **S1**, supporting information).

Experimental Methods

Wide-field fluorescence microscopy imaging coupled with AFM (JPK Instruments, Nanowizard3) was performed on an inverted optical microscope (Nikon, Eclipse Ti-U). The AFM head was mounted on top of the optical microscope. Fluorescence from the sample was collected through an objective lens (Nikon, 60×, 0.95 NA) excited by a 445 nm LED light source (Lumencor, Spectra X) through a dichroic excitation filter (Semrock, Di02-R442). Signals were recorded through an emission filter (Semrock, BLP01-458R) with an EMCCD camera (Andor, iXon 897). The exposure time for each image was adjusted to collect appropriate signals. Color images were obtained by combining three images recorded with appropriate emission filters: blue (Semrock, 451/106, FF01-451/106-25), green (Semrock, 550/88, FF01-550/88-25), and red channel (Semrock, 650/100, FF02-650/100-25), which selectively collect the fluorescence from (*R*)-**1**NDI donors, FRET pairs ((*R*)-**1**NDI - (*S*)-**2**PDI), and (*S*)-**2**PDI aggregates, respectively (Figure **1**, top), and were then merged in Image J software. Localized fluorescence spectra were recorded using the optical microscope equipped with a piezo-scanner (PI Instruments, P-545.3C8S) and a custom Labview software that allows user-defined spectra to be recorded in synchronization with a CCD spectrograph (Acton SP2356 with Spec-10 400Br/LN-eXcelon CCD detector cooled with liquid nitrogen, from Princeton Instrument). AFM images were recorded in the intermittent contact mode

(tapping) under ambient conditions using silicon cantilevers (Nanosensors, PPP-NCHR-20) with a nominal spring constant of 40 N m^{-1} and a resonance frequency of 330 kHz. Fluorescence polarization images were obtained on the same optical microscope using a fixed polarizer in the excitation light path, which selects the horizontal polarization excitation to the CCD field of view, and a rotating emission polarizer placed in the emission path. Polarized emission images and spectra were collected with the EMCCD camera or the CCD spectrograph, respectively. After correcting the geometric distortions of each image for vertical and horizontal emission polarization, and estimating the G-factor for the blue, green and red channels, the polarization parameter (P) was calculated at each image pixel using the following equation: $P = \frac{I_{||} - G \times I_{\perp}}{I_{||} + G \times I_{\perp}}$

where $I_{||}$ is the intensity of the linearly polarized emission parallel to the excitation polarization and $I_{\perp}$ is the intensity of the linearly polarized emission perpendicular to the excitation polarization.

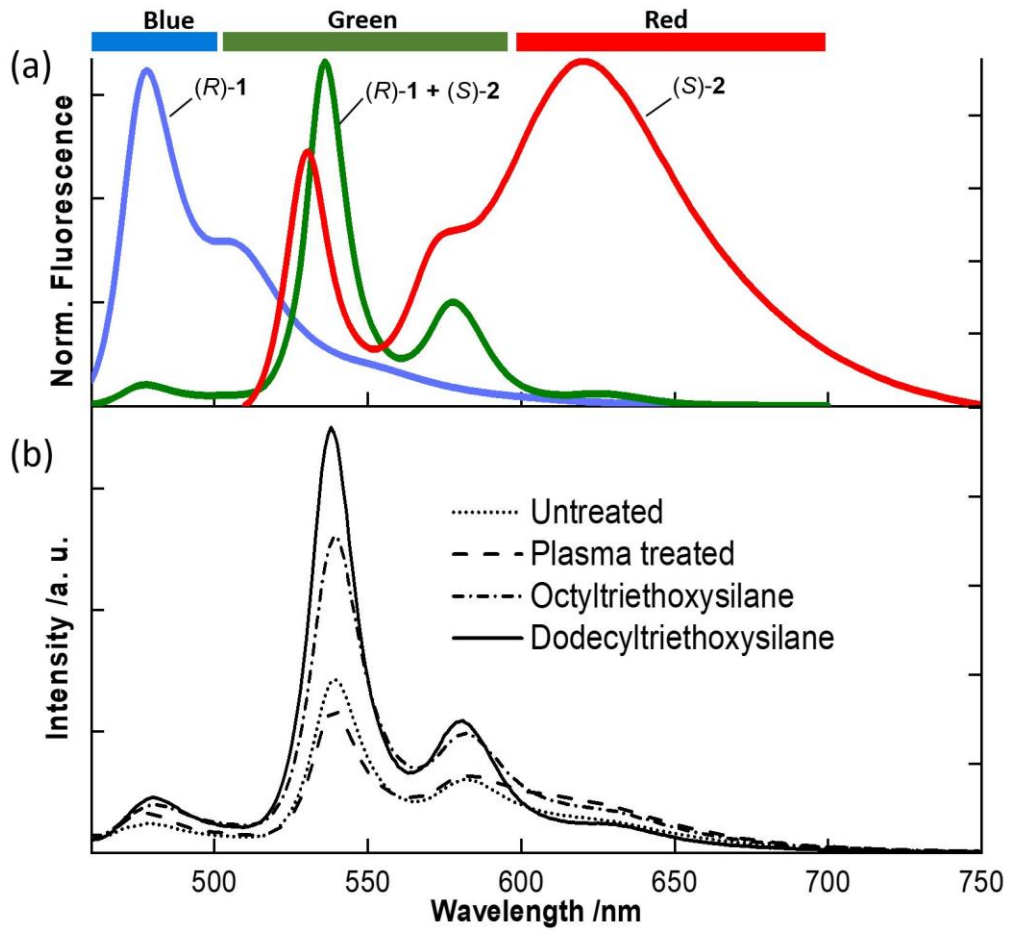

Figure 1. (a) Normalized emission spectra of (*R*)-**1**NDI (blue curve, [(*R*)-**1**] = 1.0×10^{-5}M), (*R*)-**1**NDI in presence of 1.5 mol % of (*S*)-**2**PDI (green curve, [(*R*)-**1**] =1.0×10^{-5} M, [(*S*)-**2**] = 1.5×10^{-7} M) and (*S*)-**2**PDI (red curve, [(*S*)-**2**] = 1.0×10^{-6} M) in MCH rich solution. The color-bars designates wavelength regions for emission filters and detection channels in the microscopy imaging, i.e. blue (λ_{em} < 500 nm), green (500 nm < λ_{em} <600 nm) and red (λ_{em} > 600 nm). (b) Fluorescence spectra of (*R*)-**1**NDI in presence of 1.5 mol % of (*S*)-**2**PDI ([(*R*)-**1**] = 1.0×10^{-5} M, [(*S*)-**2**] = 1.5×10^{-7} M), deposited from MCH rich solution onto different glass substrates.

3. Results and Discussion

The supramolecular nanofibers were prepared by mixing (*R*)-**1**NDI in the presence of 1.5 mol% (*S*)-**2**PDI in MCH rich solution at very low concentration ([(*R*)-**1**] = 1.0×10^{-5} M, [(*S*)-**2**] = $1.5 \times$

10^{-7} M), followed by drop casting onto an untreated glass slide. Upon selective excitation of (*R*)-**1**NDI at 445 nm, the emission spectrum showed a low-intensity emission band at 480 nm corresponding to the diethoxy-NDI unit and a major emission band peaking at 540 nm of the (*S*)-**2**PDI unit (Figure **1**b). This indicates efficient light-harvesting from (*R*)-**1**NDI nanofibers to the (*S*)-**2**PDI molecule. This light-harvesting behavior was evaluated by monitoring the relative emission intensities of (*S*)-**2**PDI at 540 nm and (*R*)-**1**NDI at 480 nm (I_{540}/I_{480}), which was approximately 6-fold when deposited on the untreated glass surface. This value is significantly lower than in the bulk solution phase (~20 fold). This efficient light-harvesting phenomenon is specific for the combination [(*R*)-**1**NDI nanofibers+(*S*)-**2**PDI] and [(*S*)-**1**NDI nanofibers+(*R*)-**2** PDI], but not those of same chirality.[46] The sample deposited on a plasma-treated glass slide showed a significantly lower I_{540}/I_{480} value (ca. 4 fold) along with a broad band above 580 nm. This red band corresponds to the aggregated emission of (*S*)-**2**PDI molecules (Figure **1**a, red line). This suggests that a significant fraction of (*S*)-**2**PDI is not associated with (*R*)-**1**NDI nanofibers on the plasma-treated glass slide.[51,52] We then examined glass slides treated with alkylsilanes, n-octyltriethoxysilane and n-dodecyltriethoxysilane (Figure **1**), as more hydrophobic substrates. A 7- and 8-fold enhancement of the relative emission intensity (I_{540}/I_{480}) was observed for the substrate surface treatment with n-octyltriethoxysilane and n-dodecyltriethoxysilane, respectively (Table **S1**, supporting information). Although the chemical origin of this significant effect of surface hydrophobicity on the energy harvesting efficiency of the supramolecular nanowires is not fully understood, we focused on the fluorescence properties of the nanofibers formed on alkylsilane-coated glass slides, which showed good reproducibility. Our host-guest light-harvesting system successfully demonstrated efficient energy transfer both in solution and when

deposited on treated glass substrates, although the relative fluorescence efficiency (I_{540}/ I_{480}) in the solvent-dispersed phase was not fully reproduced.

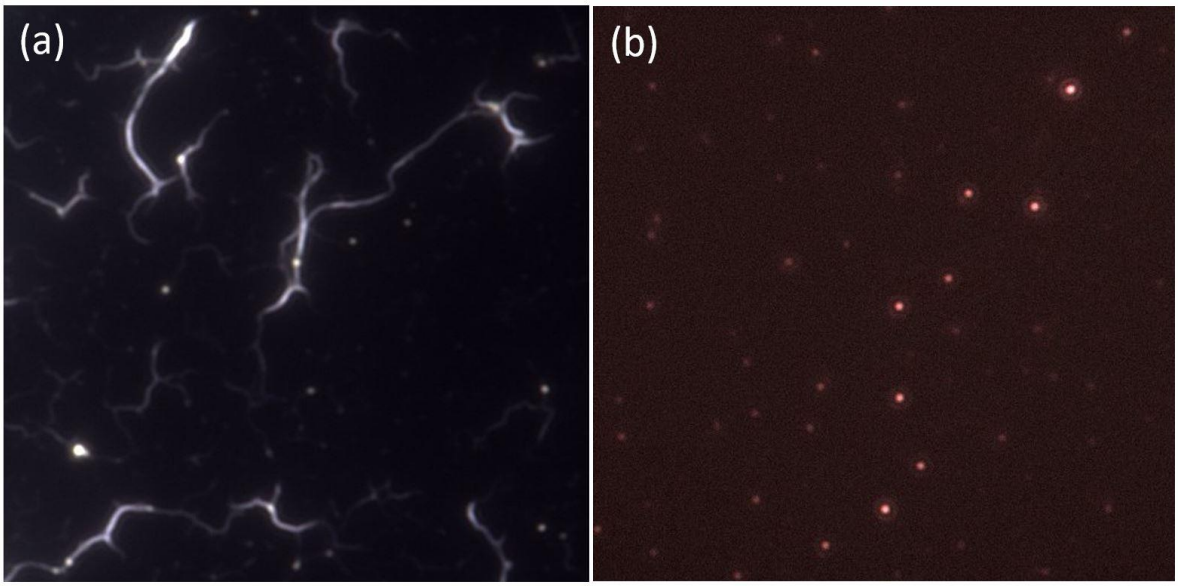

Figure 2. Fluorescence microscope images (50 × 50 μm) of (a) (*R*)-**1**NDI and (b) (*S*)-**2**PDI on alkyl-treated glass slides after drop casting in methylcyclohexane rich solution. [(*R*)-**1**] = 1.0×10^{-5} M, [(*S*)-**2**] = 1.0×10^{-7} M.

Fluorescence and topography images were then investigated using an optical microscope coupled with atomic force microscope (AFM) to visualize and characterize the emission properties and energy transfer processes on individual nanofibers. First, fluorescence microscopy images were recorded of individual samples of (*R*)-**1**NDI and (*S*)-**2**PDI, deposited on alkyl-treated glass substrates. (*R*)-**1**NDI (1.0×10^{-5} M; Figure **2**a) showed blue-emitting long nanofibers, while (*S*)-**2**PDI (1.0×10^{-7} M; Figure **2**b) formed bright red spherical fluorescent particles. These bright red spherical objects correspond to partially self-aggregated (*S*)-**2**PDI molecules, where the self-assembly likely proceeds during the solvent drying process driven by strong π–π interactions.[52,53] Although the compound **2** was previously reported to form nanofibers in MCH-rich solution, they

were not observed here under fluorescence microscopy due to the low concentration of **2** molecules, insufficient to afford the self-assembly of (*S*)-**2**PDI into nanofibers.[51,52] In addition, a well-defined network of blue-green emitting fluorescent nanofibers, accompanied by several red spots was observed in the fluorescence images of the sample (*R*)-**1**NDI in the presence of 1.5 mol % of (*S*)-**2**PDI ([(*R*)-**1**] = 1.0×10^{-5} M, [(*S*)-**2**] = 1.0×10^{-7}M) drop cast on n-octyltriethoxysilane glass slides (Figure **3**a). These uniform long nanofiber supramolecular structures are very similar to those observed in MCH-rich solution as previously characterized by transmission electron microscopy (Figure **S2**, Supporting Information).[46] Noteworthy, the bright red spherical spots were found mostly at the intersection of the (*R*)-**1**NDI nanofibers, e.g. some at region marked as I, II and III in Figure 3a. Fluorescence images of the (*R*)-**1**NDI + (*S*)-**2**PDI mixture deposited on n-dodecyltriethoxysilane-coated glass slides revealed blue-green emitting fibers along with bright red spots (Figure **S3**a, Supporting Information), similar to that of n-octyltriethoxysilane-coated glass slides. However, when deposited on uncoated glass slides, a random distribution of blue-emitting fibers was observed along with a large number of bright red spots in the background (Figure **S3**b, Supporting Information), confirming the disrupted supramolecular association of (*S*)-**2**PDI into (*R*)-**1**NDI nanofibers on the untreated glass slide. The higher compatibility of alkylsilane-coated glass slides was confirmed by fluorescence imaging studies.

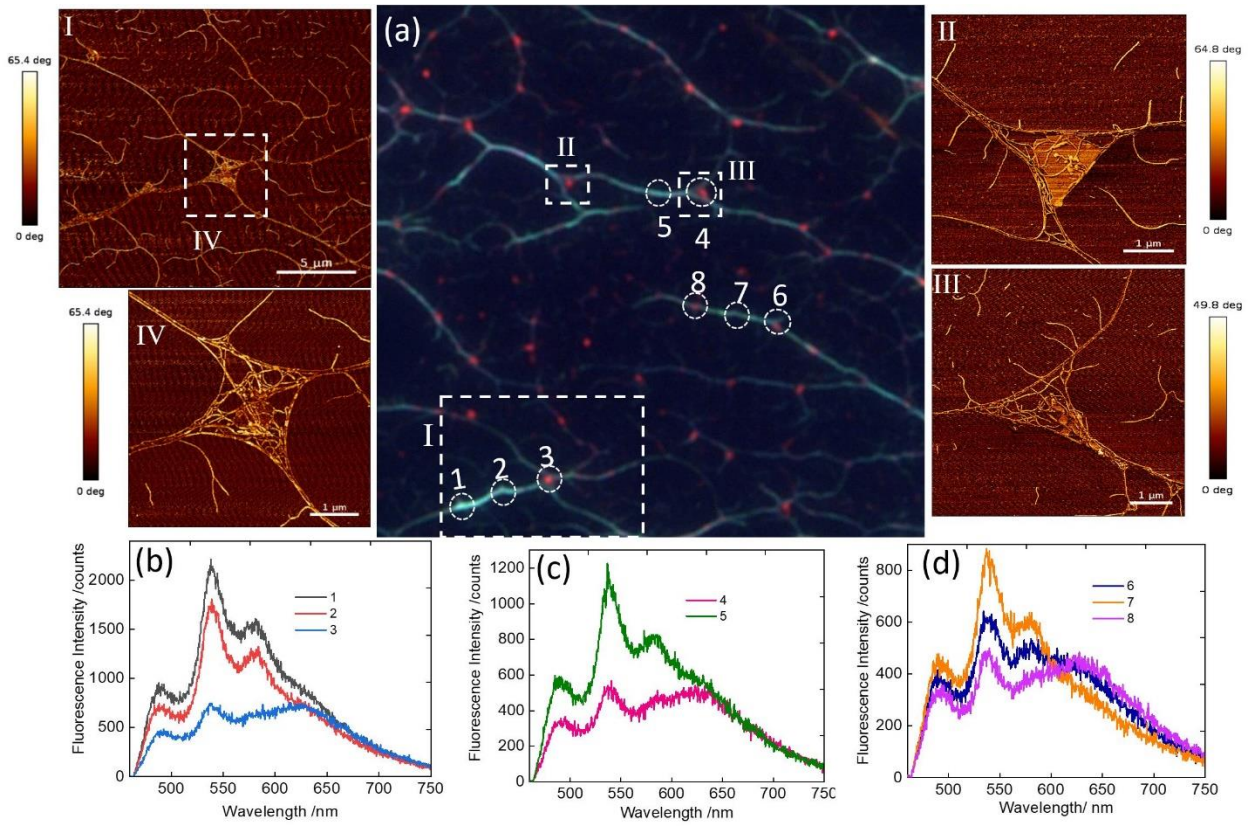

Figure 3. (a) Fluorescence microscope images (50 × 50 μm) of (*R*)-**1**NDI in presence of 1.5 mol % of (*S*)-**2**PDI drop casted on n-octyltriethoxysilane coated glass slides with AFM phase contrast images for regions I-IV of dashed squares, (b)-(d) the emission spectra at different regions 1-8 of the fibers. The color channels of fluorescence image are shown Figure 1a. [(*R*)-**1**] = 1.0×10^{-5} M, [(*S*)-**2**] = 1.0×10^{-7} M.

The blue-green fluorescent fibers and red-emitting spots were fully characterized by spectral analysis of the (*R*)-**1**NDI + (*S*)-**2**PDI mixture on n-octyltriethoxysilane-coated glass slides under excitation at 445 nm. For each position as marked with white circles 1-8 in Figure **3**a along the single nanofibers, the spectra showed weak emission at 480 nm from the (*R*)-**1**NDI units with a concomitant larger contribution of emission around 540 nm corresponding to the (*S*)-**2**PDI fluorophores. In some cases, broad emission at 640 nm from aggregated (*S*)-**2**PDI was also

observed, especially at 3, 4, 6 and 8 (Figure **3**b-d). The strong blue-green fluorescent regions (circles 1, 2, 5, and 7) showed emission essentially from the (*R*)-**1**NDI nanofibers and (*S*)-**2**PDI molecules, with the large values of the I_{540}/I_{480} ratio indicating efficient excitation energy transfer from the (*R*)-**1**NDI nanofibers to the (*S*)-**2**PDI molecules, due to uniformly distributed isolated (*S*)-**2**PDI molecules in close proximity to the nanofibers, acting as efficient acceptor sites. In contrast, the spectra of the bright red spots (circles 3, 4, 6, and 8) revealed broad emission spectra with significant suppressed (*R*)-**1**NDI emission and an intense dual emission band around 540 nm and 640 nm, respectively of (*S*)-**2**PDI units, suggesting energy transfer from (*R*)-**1**NDI nanofibers to (*S*)-**2**PDI aggregates ((*S*)-**2**PDI_{agg}) due to excess (*S*)-**2**PDI guests forming self-assembled structure. The distinct emission spectrum at different positions of the nanofibers (Figure **3**a) indicates a large diversity of the major emitting species present in the sample. The inhomogeneity of the host-guest system likely arises from the random distribution of (*S*)-**2**PDI guests on the (*R*)-**1**NDI nanofibers during the solvent drying process, when the samples were drop-cast onto alkyl-coated glass slides, since such a broad emission band around 640 nm was negligible in the solution state.[46] The dispersion of (*S*)-**2**PDI guests on the nanofibers resulted in energy transfer from (*R*)-**1**NDI nanofibers to individual (*S*)-**2**PDI units ((*S*)-**2**PDI_{mono}) due to the PDI molecules in their molecularly dispersed form similar to that in the MCH-rich solution.[46] Furthermore, energy transfer pathways from (*R*)-**1**NDI nanofibers to the self-aggregated (*S*)-**2**PDI ((*S*)-**2**PDI_{agg}) were confirmed by the red emission band specific to the deposited state. The static local environment in dry samples, contrary to the solution samples, led to the accumulation of (*S*)-**2**PDI molecules into large spherical aggregates driven by strong π–π interaction and chiral binaphthalene moiety. Moreover, the localization positioning of these spherical aggregates ((*S*)-**2**PDI_{agg}), which frequently occurred in close vicinity to the nanofibers, probably favors efficient excitation energy

transfer from (*R*)-**1**NDI fibers to individual (*S*)-**2**PDI molecular units, followed by a second energy transfer step to (*S*)-**2**PDI$_{agg}$. Spectral analysis on n-dodecyltriethoxysilane-coated glass slides (Figure **S4**, supporting information) was found to be very similar to that of n-octyltriethoxysilane-coated glass slides, suggesting that different alkylsilane modifications have comparable effects on their energy transfer efficiency. The inhomogeneous distribution of (*S*)-**2**PDI guests on the (*R*)-**1**NDI nanofibers was further confirmed by atomic force microscopy (AFM) performed on specific regions of the fluorescence microscopy image (Figure **3**a), shown as dashed squares (I-IV and Figure **S5**, Supporting Information). Indeed, AFM characterization provided more detailed insight into the nanofiber structure in the region of interest where spectral analysis was performed. A random distribution of individual fibers and bundles was observed in the AFM images. The fibers showed a wide variety of sizes and branching topology. Notably, many nanofibers with low brightness, below the resolution and detection limit of fluorescence microscopy imaging, were visible in the AFM images. Highly emissive regions were found to be composed of several thin fibers (~8 nm wide) clustered into bundles of 20-100 nm width (Figure **3** I-IV), supporting our previous TEM studies in the solution phase.[46] Additionally, the occurrence of bright red spots at the branching points of the thin nanofibers is quite apparent in these AFM images (Figure **3** II-IV). These red-emitting objects were found to consist of the diffusion of relatively largely disordered materials connecting the network of thin fibers, corresponding to highly concentrated (*S*)-**2**PDI guest molecules wrapped within the intertwined thin (*R*)-**1**NDI nanofibers (Figure **3** II-III-IV; Figure **S5**, Supporting Information). Although the resolution of the AFM measurements was not sufficient to fully characterize the local distribution of (*S*)-**2**PDI molecules on the (*R*)-**1**NDI nanofibers, each red-emitting spot was interestingly associated with multiple branching junctions in the nanofiber networks. This nanofiber network contained small spherical nano-objects or larger

nanolayers, likely composed of (*S*)-**2**PDI aggregates (Figure **S5**, Supporting Information). The AFM images suggest that the presence of repeated branching and coiling of the thin nanofibers may act as packing defects, suppressing both the long-range exciton hopping along the (*R*)-**1**NDI nanofibers and energy transfer efficiency compared to the solution phase.[47] Moreover, the (*R*)-**1**NDI and (*S*)-**2**PDI host-guest system deposited on glass is expected to be more rigid than in the solution phase. The random but less uniform distribution of (*S*)-**2**PDI guest on (*R*)-**1**NDI nanofibers during the solvent drying process upon drop-casting onto glass slides might result in a variety of fixed localized positions and orientations of some (*S*)-**2**PDI molecules on (*R*)-**1**NDI fibers. Some of these geometries may be less compatible for energy transfer from (*R*)-**1**NDI nanofibers to (*S*)-**2**PDI molecules, thus reducing the energy transfer efficiency, compared to the solution phase. Finally, the presence of partially self-aggregated (*S*)-**2**PDI molecules in the vicinity of (*R*)-**1**NDI nanofibers, which interact effectively with the (*R*)-**1**NDI donors, favors excitation energy transfer from nanofibers to (*S*)-**2**PDI aggregates ((*S*)-**2**PDI_{agg}) acting as acceptors.

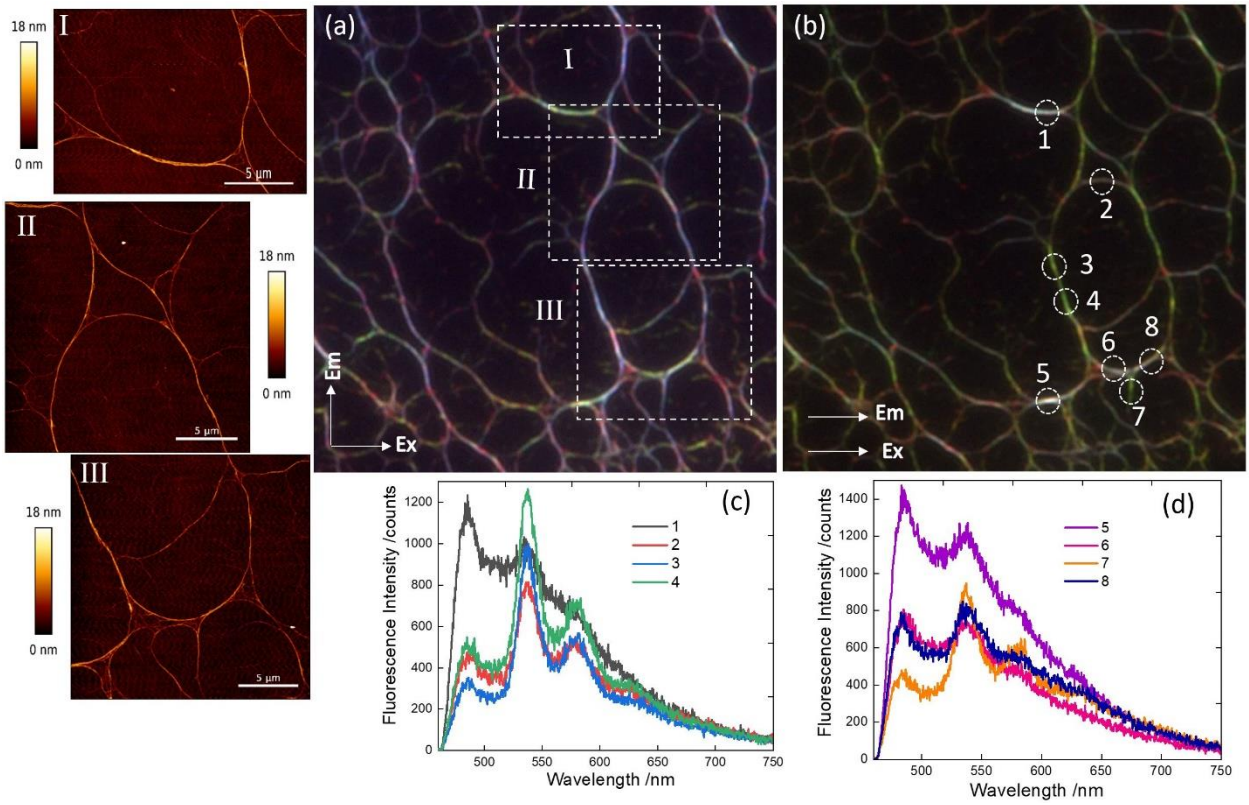

Figure 4. Fluorescence microscopy (50 × 50 μm) of (*R*)-**1**NDI in the presence of 1.5 mol % of (*S*)-**2**PDI drop casted on octyltriethoxysilane coated glass slides upon excitation with horizontally polarized light (λ_{ex} = 445nm), (a) perpendicular $I_{\perp}$, and (b) parallel $I_{\parallel}$ collected emission with respect to the excitation laser beam polarization respectively, (c, d) emission spectra of specified regions of the fibers (1-8) upon horizontal emission polarization ($I_{\parallel}$), and (I - III) AFM images of the marked regions on (a) with white dashed squares.

Fluorescence polarization is a powerful technique for characterizing energy transfer (ET), internal packing, and chromophore orientation in supramolecular assemblies in solution,[11,26,46,47,53,54] as well as in the solid phase.[55] When combined with fluorescence microscopy imaging (referred to as fluorescence polarization imaging),[56,57] it can be used to visualize and characterize energy transfer dynamics in such anisotropic assemblies.[44,45] The anisotropy in our light-harvesting supramolecular assembly was confirmed by fluorescence polarization (*P*) imaging of individual

nanofibers under excitation with linearly polarized light (Figure **4**). Molecules selectively absorb linearly polarized light when the absorption dipole moments of (*R*)-**1**NDI or (*S*)-**2**PDI, oriented along their long molecular axis, are parallel to the polarization axis of the excitation beam (photo-selection). The (*R*)-**1**NDI + (*S*)-**2**PDI mixture sample in the deposited state on n-octyltriethoxysilane-coated glass slides was excited with a horizontally linear polarized light (λ_{ex} = 445 nm, Figure **S6**, Supporting Information). In our microscopy setup, a rotatable polarizer was placed in the emission path and oriented either perpendicular (Figure **4**a, $I_{\perp}$) or parallel (Figure **4**b, $I_{\parallel}$) to the direction of the horizontally polarized excitation laser beam. Interestingly, a clear fluorescence contrast was observed in Figures **4**a and **4**b. The more pronounced blue emission was observed for the nanofibers oriented along the vertical (north/south) direction in Figure **4**a, which became green emitting fibers in Figure **4**b. The color contrast was partially reversed between the north/south (vertical) and east/west (horizontal) oriented nanofibers (Figure **4**b), with more greenish emission in in Figure **4**b ($I_{\parallel}$) and more blueish emission in Figure **4**a ($I_{\perp}$), suggesting a strong dependence of the polarized emission on the orientation of the nanofibers growth axis. As discussed earlier, red spots appear at some nanofiber junctions, and no significant change in emission color was observed when the emission polarization direction was changed from perpendicular to parallel to the excitation beam, indicating a rather random orientation of (*S*)-**2**PDI aggregates in the vicinity of the nanofibers, resulting in unpolarized emission. The AFM images on displayed regions (I-III) in Figure **4**a ensured the reliability of the polarization studies by optical microscopy without any noticeable artifacts. Indeed, the AFM images showed well-defined straight long fibers oriented at specific angles to each other, without any break in the nanofiber networks upon coiling or branching. On the one hand, the spectra at the green-emitting regions 3, 4, and 7 (Figure **4**b, white circles), corresponding to the vertically oriented fibers (north/south) to

that of the excitation polarization beam, showed an intense emission maximum centered at 540 nm with the enhanced relative fluorescence intensity (I_{540}/I_{480}), indicating the preferential green emission of the (*S*)-**2**PDI guest units by efficient energy transfer from the vertically oriented fibers. On the other hand, the spectra of horizontally (east/west) oriented fibers on regions 1 and 5 (Figure **4**b, white circles) displayed higher intensity at 480 nm in the blue spectral region, suggesting the most prominent blue-polarized emission from (*R*)-**1**NDI fibers. The slightly tilted fibers at sites 2, 5, 6, and 8 (Figure **4**b, white circles) showed an intermediate ratio of I_{540}/I_{480} compared to the east/west oriented fibers. Hence, the different orientations of the fibers with respect to the excitation beam have a direct influence on their polarized emission properties. Practically, the deposited samples of (*R*)-**1**NDI + (*S*)-**2**PDI mixture on glass substrate show supramolecular nanofibers with a large diversity of orientations (θ) and result in many directions of transition moments of (*R*)-**1**NDI and (*S*)-**2**PDI chromophores with respect to the sample reference axes, hence a wide variety of polarization values (*P*). In well-ordered regions, the (*S*)-**2**PDI fluorophores are expected to be incorporated on the (*R*)-**1**NDI nanofibers and can be excited either directly or by energy transfer from the (*R*)-**1**NDI molecules. However, in regions where disorder is dominant, the (*S*)-**2**PDI molecules have limited interactions and proximity with the fibers, and energy transfer from (*R*)-**1**NDI nanofibers to (*S*)-**2**PDI molecules is not favored.

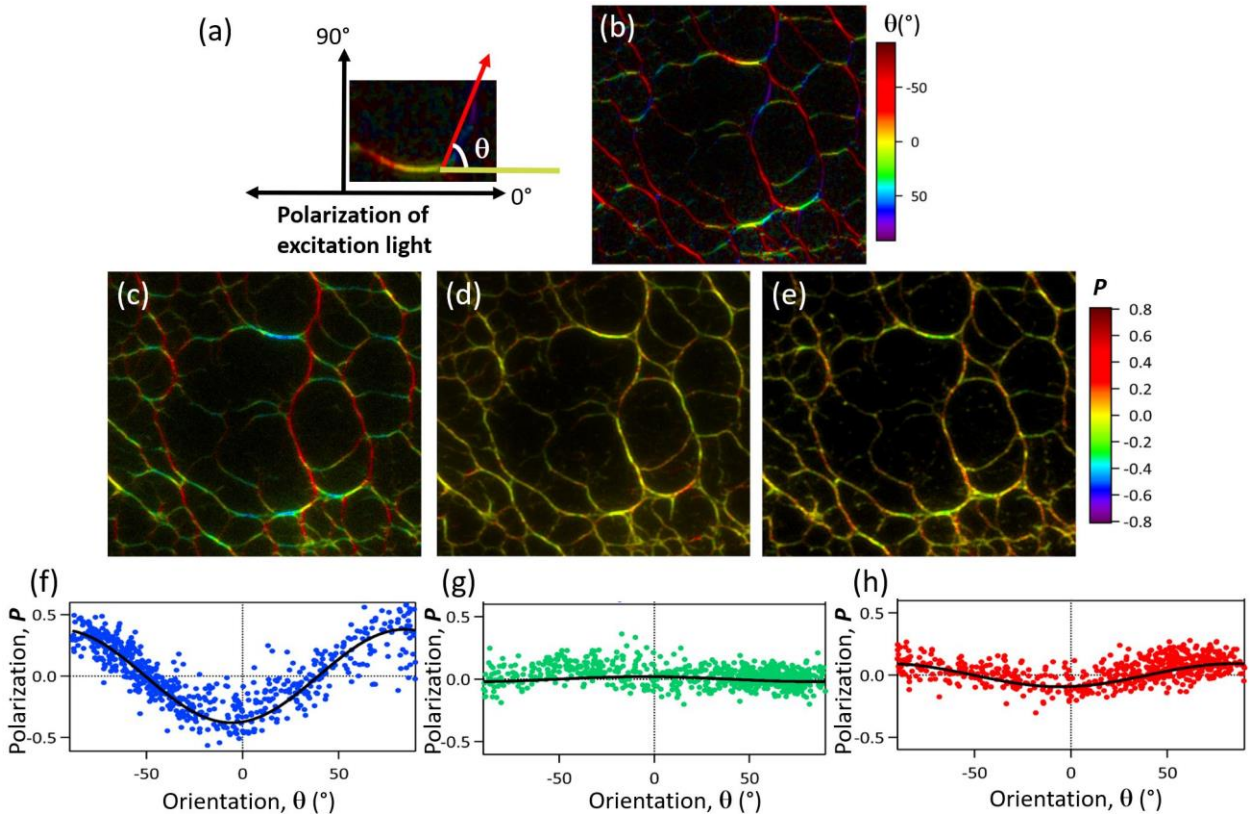

Figure 5. (a) The schematic representation of the angle of the fiber growth axis (θ) to the polarization of the excitation beam, (b) orientation color image (50 × 50 μm) of (*R*)-**1**NDI in the presence of 1.5 mol% of (*S*)-**2**PDI from ImageJ software with orientationJ as a plugin, the fluorescence polarization color image corresponding to the emission filters for (c) $\lambda_{em} < 500$ nm, (d) 500 nm $< \lambda_{em} <$ 600 nm and (e) $\lambda_{em} > 600$ nm respectively and their linear plot of polarization (*P*) as a function of orientation (θ) at (f) $\lambda_{em} < 500$ nm (blue dots, (*R*)-**1**NDI), (g) 500 nm $< \lambda_{em} <$ 600 nm (green dots, (*S*)-**2**PDI$_{mono}$), and (h) $\lambda_{em} > 600$ nm (red dots, (*S*)-**2**PDI$_{agg}$), respectively, when excited with horizontally polarized light (λ_{ex} = 445nm). (Solid lines are obtained by fitting *P* with a sinusoidal function).

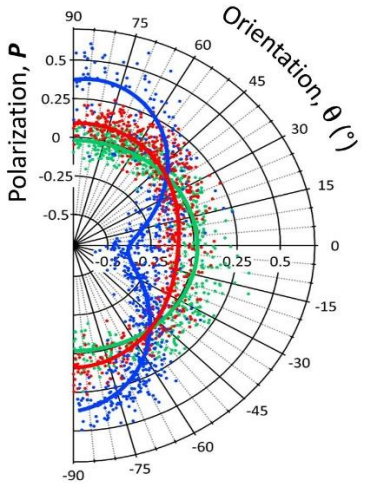

Figure 6. Polar plots of the polarization (*P*) as a function of the angle of the nanofiber growth axis (θ) to the direction of the excitation laser polarization at λ_{em} < 500 nm (blue dots, (*R*)-**1**NDI), 500 nm < λ_{em} < 600 nm (green dots, (*S*)-**2**PDI$_{mono}$), λ_{em} > 600 nm (red dots, (*S*)-**2**PDI$_{agg}$), respectively, when excited with horizontally polarized light (λ_{ex} = 445nm). (Solid lines are obtained by fitting *P* with a sinusoidal function).

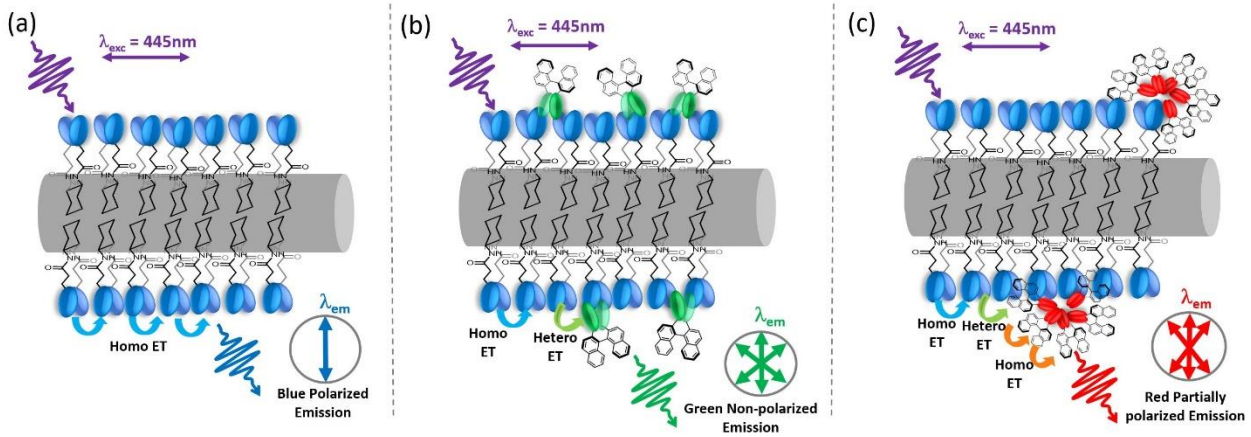

Scheme 2. Schematic representation of the proposed spatial organization of (*R*)-**1**NDI (in blue, a), (*S*)-**2**PDI$_{mono}$ (green, b), and (*S*)-**2**PDI$_{agg}$ (red, c) on east/west oriented fibers (θ = 0°, horizontal to the excitation laser polarization beam) and their photophysical process.

In general, the polarization value *P* can vary from -1 to +1, corresponding to perpendicular to parallel emission polarization with respect to the excitation polarization. When $P = 0$, the emission is not polarized towards a specific direction. The polarization images displayed in Figure **5** (a-e) reveal a clear correlation between the *P* value of the nanofiber emission and the angle of the nanofiber growth axis (θ) to the orientation of the excitation polarization. For the (*R*)-**1**NDI and (*S*)-**2**PDI mixture deposited on coated glass substrates, the emission polarization images (Figure **5**c) demonstrates qualitatively the strong orientation dependence of the blue emission polarization: north-south vertically-oriented fibers (resp. east-west horizontally-oriented fibers) show positive (resp. negative) *P* values. This corresponds to a positively polarized emission ($P = + 0.38 \pm 10$) for north/south oriented fibers, i.e. $\theta = 90°$ (vertical) to the excitation polarization (Figure **5**f), and negatively polarized emission ($P = - 0.38 \pm 10$) for east/west oriented fibers ($\theta = 0°$, horizontal). Also, *P* varies in a sinusoidal manner between these two extremes ($P = \pm 0.38$) for the fibers oriented with an intermediate angle θ (Figures **5**f and **6**, blue lines). The strongly polarized blue emission ($\lambda_{em} < 500$ nm) from the nanofibers varies strongly with the angle of fiber orientation (θ), indicating a high degree of intermolecular ordering and a preferential average orientation of the (*R*)-**1**NDI molecular units along the nanofiber. In addition, a negative polarization for horizontally (north/south) oriented fibers and, conversely, a positive polarization for vertically (east/west) oriented fibers indicates that the (*R*)-**1**NDI units emit strong blue polarized light perpendicular to the long axis of the fibers when excited with linear polarization. Therefore, (*R*)-**1**NDI molecular units are self-assembled in a perpendicular manner to the long axis of the fiber, with some degree of angle variations as highlighted by the maximum polarization amplitude (± 0.38) lower than 1.0 for ideally perpendicular (*R*)-**1**NDI chromophores. The efficient exciton hopping within the (*R*)-**1**NDI chromophores ((*R*)-**1**NDI→(*R*)-**1**NDI homo-transfer), leading to partial depolarization of

the emission on ultrafast timescales (<20 ps) but residual anisotropy levels on longer timescales (few ns), has already been demonstrated in our previous work[47] (Scheme **2**a). In contrast, the plot of *P* vs θ (Figure **5**g and **6**, green lines) remains close to *P* = 0 for the green emission region (λ_{em} = 500-600nm) which corresponds to (*S*)-**2**PDI_{mono} emission. This result indicates that a complete depolarization of the (*S*)-**2**PDI_{mono} is observed upon sensitization by the (*R*)-**1**NDI chromophores (efficient (*R*)-**1**NDI → (*S*)-**2**PDI hetero-transfer), without any preferred orientation of the (*S*)-**2**PDI guest with respect to the nanofiber orientation. Given the highly enantioselective binding of the (*S*)-**2**PDI guest molecules to the nanofibers[47] and their bulkiness, the loss of emission polarization of (*S*)-**2**PDI_{mono} can be attributed to a local disruption of the overall helicoidal molecular arrangement upon guest binding (Scheme **2**b). Surprisingly, a moderately polarized red emission (*P* = **-** 0.10 ± 10, θ = 0°) of (*S*)-**2**PDI_{agg} (λ_{em} > 600 nm) was observed when sensitized with (*R*)-**1**NDI (λ_{ex} = 445nm) (Figure **5**h, red lines). This weak dependence of the red emission polarization (Figure **6**, red lines) on the angle of fiber orientation (θ) suggests a partial molecular ordering of the (*S*)-**2**PDI units in their aggregates, driven by the strong π–π interaction and the chiral binaphthalene moiety that occur in close proximity to the nanofibers. The efficient energy transfer from horizontally oriented (*R*)-**1**NDI nanofibers (θ = 0°) to a PDI molecular unit of spherical (*S*)-**2**PDI_{agg} ((*R*)-**1**NDI →(*S*)-**2**PDI hetero-transfer), followed by possible exciton hopping ((*S*)-**2**PDI→(*S*)-**2**PDI homo-transfer) within (*S*)-**2**PDI_{agg}, could effectively lead to a weak red emission polarization, slightly preferentially perpendicular to the nanofiber long axis (parallel to the (*R*)-**1**NDI orientation) (Scheme **2**c).

4. Conclusion

In conclusion, this work demonstrates the efficient light-harvesting property of supramolecular nanofiber assemblies of (*R*)-**1**NDI towards (*S*)-**2**PDI$_{agg}$ guest molecules, as visualized by fluorescence microscopy. The lower relative fluorescence efficiency of energy transfer in the deposited samples compared to that in the bulk solution is attributed to inhomogeneities and packing defects present in the (*R*)-**1**NDI nanofibers, as evidenced by AFM and spectroscopy analyses. Uneven distribution of (*S*)-**2**PDI molecules on the (*R*)-**1**NDI nanofibers resulted in energy transfer from (*R*)-**1**NDI fibers to isolated PDI molecules ((*S*)-**2**PDI$_{mono}$) as well as their partially self-aggregates ((*S*)-**2**PDI$_{agg}$). Fluorescence polarization imaging revealed a strong dependence of polarized emission on nanofiber orientation. The nanofibers emit strongly polarized blue emission, indicating that the (*R*)-**1**NDI molecular units are stacked perpendicular to the long axis of the fibers. Weakly polarized emission at emission wavelength region higher than 500 nm indicates that the binding of (*S*)-**2**PDI$_{mono}$ to the nanofibers has no preferred orientation, while its spherical self-aggregates (*S*)-**2**PDI$_{agg}$ interact more efficiently with the periphery of the fibers, which exhibit partial alignment, explaining the heterogeneity and differential energy transfer efficiency of our light-harvesting system. This finding highlights the importance of microscopy with spectral and polarization analysis for the comprehensive characterization of multicomponent light-harvesting systems and the identification of key features such as disorder, heterogeneity, and anisotropy in their interfaces, which can be manipulated/controlled to enhance the performance of future optoelectronic materials.

ASSOCIATED CONTENT

Supporting Information. Experimental details and supporting data including additional spectroscopy data, TEM images, AFM images, fluorescence microscopy images (PDF file).

AUTHOR INFORMATION

Tsuyoshi Kawai- Division of Material Science, Graduate School of Science and Technology, Nara Institute of Science and Technology (NAIST), Ikoma, Nara 630-0192, Japan.

*Email: tkawai@ms.naist.jp (T.K.)

Rémi Métivier- Université Paris-Saclay, ENS Paris-Saclay, CNRS, PPSM, 91190 Gif-sur-Yvette, France.

*Email: remi.metivier@ens-paris-saclay.fr (R.M.)

Ramarani Sethy- Division of Material Science, Graduate School of Science and Technology, Nara Institute of Science and Technology (NAIST), Ikoma, Nara 630-0192, Japan.

Université Paris-Saclay, ENS Paris-Saclay, CNRS, PPSM, 91190 Gif-sur-Yvette, France.

Takuya Nakashima- Division of Material Science, Graduate School of Science and Technology, Nara Institute of Science and Technology (NAIST), Ikoma, Nara 630-0192, Japan.

Department of Chemistry, Graduate School of Science, Osaka Metropolitan University, Sumiyoshi-ku, Osaka 558-8585, Japan.

Arnaud Brosseau- Université Paris-Saclay, ENS Paris-Saclay, CNRS, PPSM, 91190 Gif-sur-Yvette, France (present address: Moltech-Anjou, CNRS, Université d'Angers, France).

CONFLICTS OF INTEREST

The authors declare no conflicts of interest.

ACKNOWLEDGMENTS

This research was partly supported by the CNRS International Research Project Nanosynergetics (R.M.), JSPS KAKENHI grant numbers JP23H04876 (T.K.) and JP22H05134 (T.N.) for Transformative Research Areas (A) “Materials Science of Meso-Hierarchy” and “Revolution of Chiral Materials Science using Helical Light”, respectively, and JP22H02052 (T.K.) for Grant-in-Aid for Scientific Research (B).

REFERENCES

(1) Brixner, T.; Hildner, R.; Köhler, J.; Lambert, C.; Würthner, F. Exciton Transport in Molecular Aggregates – From Natural Antennas to Synthetic Chromophore Systems. *Adv. Energy Mater.* **2017**, *7* (16), 1700236. https://doi.org/10.1002/aenm.201700236.

(2) Scholes, G. D.; Rumbles, G. Excitons in Nanoscale Systems. *Nat. Mater.* **2006**, *5* (9), 683–696. https://doi.org/10.1038/nmat1710.

(3) Laquai, F.; Park, Y.-S.; Kim, J.-J.; Basché, T. Excitation Energy Transfer in Organic Materials: From Fundamentals to Optoelectronic Devices. *Macromol. Rapid Commun.* **2009**, *30* (14), 1203–1231. https://doi.org/10.1002/marc.200900309.

(4) Wittmann, B.; Wenzel, F. A.; Wiesneth, S.; Haedler, A. T.; Drechsler, M.; Kreger, K.; Köhler, J.; Meijer, E. W.; Schmidt, H.-W.; Hildner, R. Enhancing Long-Range Energy Transport in Supramolecular Architectures by Tailoring Coherence Properties. *J. Am. Chem. Soc.* **2020**, *142* (18), 8323–8330. https://doi.org/10.1021/jacs.0c01392.

(5) Fleming, G. R.; Schlau-Cohen, G. S.; Amarnath, K.; Zaks, J. Design Principles of Photosynthetic Light-Harvesting. *Faraday Discuss.* **2012**, *155* (0), 27–41. https://doi.org/10.1039/C1FD00078K.

(6) Senge, M. O.; Ryan, A. A.; Letchford, K. A.; MacGowan, S. A.; Mielke, T. Chlorophylls, Symmetry, Chirality, and Photosynthesis. *Symmetry* **2014**, *6* (3), 781–843. https://doi.org/10.3390/sym6030781.

(7) Pullerits, T.; Sundström, V. Photosynthetic Light-Harvesting Pigment−Protein Complexes: Toward Understanding How and Why. *Acc. Chem. Res.* **1996**, *29* (8), 381–389. https://doi.org/10.1021/ar950110o.

(8) Choi, M.-S.; Yamazaki, T.; Yamazaki, I.; Aida, T. Bioinspired Molecular Design of Light-Harvesting Multiporphyrin Arrays. *Angew. Chem. Int. Ed.* **2004**, *43* (2), 150–158. https://doi.org/10.1002/anie.200301665.

(9) Jiahong, L.; Jialu, S.; Chenhui, P.; Guoze, Y. The Materials and Application of Artificial Light Harvesting System Based on Supramolecular Self-Assembly. *ChemistrySelect* **2023**, *8* (3), e202202979. https://doi.org/10.1002/slct.202202979.

(10) Miyatake, T.; Tamiaki, H. Self-Aggregates of Natural Chlorophylls and Their Synthetic Analogues in Aqueous Media for Making Light-Harvesting Systems. *Coord. Chem. Rev.* **2010**, *254* (21), 2593–2602. https://doi.org/10.1016/j.ccr.2009.12.027.

(11) Nakashima, T.; Kimizuka, N. Light-Harvesting Supramolecular Hydrogels Assembled from Short-Legged Cationic L-Glutamate Derivatives and Anionic Fluorophores. *Adv. Mater.* **2002**, *14* (16), 1113–1116. https://doi.org/10.1002/1521-4095(20020816)14:16<1113::AID-ADMA1113>3.0.CO;2-U.

(12) Ajayaghosh, A.; Praveen, V. K.; Vijayakumar, C.; George, S. J. Molecular Wire Encapsulated into π Organogels: Efficient Supramolecular Light-Harvesting Antennae with Color-Tunable Emission. *Angew. Chem. Int. Ed.* **2007**, *46* (33), 6260–6265. https://doi.org/10.1002/anie.200701925.

(13) Furumaki, S.; Vacha, F.; Hirata, S.; Vacha, M. Bacteriochlorophyll Aggregates Self-Assembled on Functionalized Gold Nanorod Cores as Mimics of Photosynthetic Chlorosomal Antennae: A Single Molecule Study. *ACS Nano* **2014**, *8* (3), 2176–2182. https://doi.org/10.1021/nn500224v.

(14) Balaban, T. S. Tailoring Porphyrins and Chlorins for Self-Assembly in Biomimetic Artificial Antenna Systems. *Acc. Chem. Res.* **2005**, *38* (8), 612–623. https://doi.org/10.1021/ar040211z.

(15) Sforazzini, G.; Kahnt, A.; Wykes, M.; Sprafke, J. K.; Brovelli, S.; Montarnal, D.; Meinardi, F.; Cacialli, F.; Beljonne, D.; Albinsson, B.; Anderson, H. L. Synthesis and Photophysics of Coaxial Threaded Molecular Wires: Polyrotaxanes with Triarylamine Jackets. *J. Phys. Chem. C* **2014**, *118* (8), 4553–4566. https://doi.org/10.1021/jp500624q.

(16) Eisele, D. M.; Knoester, J.; Kirstein, S.; Rabe, J. P.; Vanden Bout, D. A. Uniform Exciton Fluorescence from Individual Molecular Nanotubes Immobilized on Solid Substrates. *Nat. Nanotechnol.* **2009**, *4* (10), 658–663. https://doi.org/10.1038/nnano.2009.227.

(17) Röger, C.; Müller, M. G.; Lysetska, M.; Miloslavina, Y.; Holzwarth, A. R.; Würthner, F. Efficient Energy Transfer from Peripheral Chromophores to the Self-Assembled Zinc Chlorin Rod Antenna: A Bioinspired Light-Harvesting System to Bridge the "Green Gap." *J. Am. Chem. Soc.* **2006**, *128* (20), 6542–6543. https://doi.org/10.1021/ja0584469.

(18) Haldar, R.; Jakoby, M.; Mazel, A.; Zhang, Q.; Welle, A.; Mohamed, T.; Krolla, P.; Wenzel, W.; Diring, S.; Odobel, F.; Richards, B. S.; Howard, I. A.; Wöll, C. Anisotropic Energy Transfer in Crystalline Chromophore Assemblies. *Nat. Commun.* **2018**, *9* (1), 4332. https://doi.org/10.1038/s41467-018-06829-3.

(19) Ahmed, S.; Kumar, A.; Mukherjee, P. S. Tetraphenylethene-Based Emissive Pt(II) Coordination Polymer toward Artificial Light-Harvesting Systems with Sequential Energy Transfer. *Chem. Mater.* **2022**, *34* (21), 9656–9665. https://doi.org/10.1021/acs.chemmater.2c02409.

(20) Rajak, A.; Das, A. Cascade Energy Transfer and White-Light Emission in Chirality-Controlled Crystallization-Driven Two-Dimensional Co-Assemblies from Donor and Acceptor Dye-Conjugated Polylactides. *Angew. Chem. Int. Ed.* **2023**, *62* (49), e202314290. https://doi.org/10.1002/anie.202314290.

(21) Han, Y.; Zhang, X.; Ge, Z.; Gao, Z.; Liao, R.; Wang, F. A Bioinspired Sequential Energy Transfer System Constructed via Supramolecular Copolymerization. *Nat. Commun.* **2022**, *13* (1), 3546. https://doi.org/10.1038/s41467-022-31094-w.

(22) Chen, X.-M.; Chen, X.; Hou, X.-F.; Zhang, S.; Chen, D.; Li, Q. Self-Assembled Supramolecular Artificial Light-Harvesting Nanosystems: Construction, Modulation, and Applications. *Nanoscale Adv.* **2023**, *5* (7), 1830–1852. https://doi.org/10.1039/D2NA00934J.

(23) Yuan, Y.-X.; Zhang, J.-N.; Wang, J.-R.; Li, K.; Zang, S.-Q. Chiral Silver Cluster-Based Light-Harvesting Systems: Enantioselective Chirality Transfer and Amplified Circularly

Polarized Luminescence. *Chem* **2024**, *10* (6), 1766–1782. https://doi.org/10.1016/j.chempr.2024.01.028.

(24) Schulz, A.; Fröhlich, R.; Jayachandran, A.; Schneider, F.; Stolte, M.; Brixner, T.; Würthner, F. Panchromatic Light-Harvesting Antenna by Supramolecular Exciton Band Engineering for Heteromeric Dye Foldamer. *Chem* **2024**, *10* (9), 2887–2900. https://doi.org/10.1016/j.chempr.2024.05.023.

(25) Mu, B.; Hao, X.; Luo, X.; Yang, Z.; Lu, H.; Tian, W. Bioinspired Polymeric Supramolecular Columns as Efficient yet Controllable Artificial Light-Harvesting Platform. *Nat. Commun.* **2024**, *15* (1), 903. https://doi.org/10.1038/s41467-024-45252-9.

(26) Cheriya, R. T.; Mallia, A. R.; Hariharan, M. Light Harvesting Vesicular Donor–Acceptor Scaffold Limits the Rate of Charge Recombination in the Presence of an Electron Donor. *Energy Environ. Sci.* **2014**, *7* (5), 1661–1669. https://doi.org/10.1039/C3EE43293A.

(27) Camacho, R.; Thomsson, D.; Yadav, D.; Scheblykin, I. G. Quantitative Characterization of Light-Harvesting Efficiency in Single Molecules and Nanoparticles by 2D Polarization Microscopy: Experimental and Theoretical Challenges. *Chem. Phys.* **2012**, *406*, 30–40. https://doi.org/10.1016/j.chemphys.2012.03.001.

(28) Camacho, R.; Tubasum, S.; Southall, J.; Cogdell, R. J.; Sforazzini, G.; Anderson, H. L.; Pullerits, T.; Scheblykin, I. G. Fluorescence Polarization Measures Energy Funneling in Single Light-Harvesting Antennas—LH2 vs Conjugated Polymers. *Sci. Rep.* **2015**, *5* (1), 15080. https://doi.org/10.1038/srep15080.

(29) Zhong, J.; Zhao, T.; Liu, M. Fluorescence Microscopic Visualization of Functionalized Hydrogels. *NPG Asia Mater.* **2022**, *14* (1), 1–23. https://doi.org/10.1038/s41427-022-00376-6.

(30) Wu, X.; Barner-Kowollik, C. Fluorescence-Readout as a Powerful Macromolecular Characterisation Tool. *Chem. Sci.* **2023**, *14* (45), 12815–12849. https://doi.org/10.1039/D3SC04052F.

(31) Pujals, S.; Feiner-Gracia, N.; Delcanale, P.; Voets, I.; Albertazzi, L. Super-Resolution Microscopy as a Powerful Tool to Study Complex Synthetic Materials. *Nat. Rev. Chem.* **2019**, *3* (2), 68–84. https://doi.org/10.1038/s41570-018-0070-2.

(32) Zhang, S.; Fan, D.; Yan, Q.; Lu, Y.; Wu, D.; Fu, B.; Zhao, M. Single-Molecule Fluorescence Imaging of Photocatalytic Nanomaterials. *J. Mater. Chem. A* **2024**, *12* (31), 19627–19662. https://doi.org/10.1039/D4TA02347A.

(33) Ameloot, R.; Vermoortele, F.; Hofkens, J.; De Schryver, F. C.; De Vos, D. E.; Roeffaers, M. B. J. Three-Dimensional Visualization of Defects Formed during the Synthesis of Metal–Organic Frameworks: A Fluorescence Microscopy Study. *Angew. Chem. Int. Ed.* **2013**, *52* (1), 401–405. https://doi.org/10.1002/anie.201205627.

(34) Ohzono, T.; Katoh, K.; Fukuda, J. Fluorescence Microscopy Reveals Molecular Localisation at Line Defects in Nematic Liquid Crystals. *Sci. Rep.* **2016**, *6* (1), 36477. https://doi.org/10.1038/srep36477.

(35) Gutiérrez, M.; Zhang, Y.; Tan, J.-C. Confinement of Luminescent Guests in Metal–Organic Frameworks: Understanding Pathways from Synthesis and Multimodal Characterization to Potential Applications of LG@MOF Systems. *Chem. Rev.* **2022**, *122* (11), 10438–10483. https://doi.org/10.1021/acs.chemrev.1c00980.

(36) Sun, M.-J.; Liu, Y.; Yan, Y.; Li, R.; Shi, Q.; Zhao, Y. S.; Zhong, Y.-W.; Yao, J. In Situ Visualization of Assembly and Photonic Signal Processing in a Triplet Light-Harvesting Nanosystem. *J. Am. Chem. Soc.* **2018**, *140* (12), 4269–4278. https://doi.org/10.1021/jacs.7b12519.

(37) Shi, X.; Zhao, S.; Wang, F.; Jiang, Q.; Zhan, C.; Li, R.; Zhang, R. Optical Visualization and Imaging of Nanomaterials. *Nanoscale Adv.* **2021**, *3* (4), 889–903. https://doi.org/10.1039/D0NA00945H.

(38) Aoki, H.; Mori, K.; Ito, S. Conformational Analysis of Single Polymer Chains in Three Dimensions by Super-Resolution Fluorescence Microscopy. *Soft Matter* **2012**, *8* (16), 4390–4395. https://doi.org/10.1039/C2SM07227K.

(39) Garcia, A. I.; Blum, S. A. Polymer Molecular Weight Determination via Fluorescence Lifetime. *J. Am. Chem. Soc.* **2022**, *144* (49), 22416–22420. https://doi.org/10.1021/jacs.2c10036.

(40) López, P. A.; Pham, V. H. B.; Blum, S. A. A General Autofluorescence Method to Characterize Polymerization Progress. *Angew. Chem.* **2023**, *135* (29), e202304618. https://doi.org/10.1002/ange.202304618.

(41) Guan, W.; Wang, S.; Lu, C.; Tang, B. Z. Fluorescence Microscopy as an Alternative to Electron Microscopy for Microscale Dispersion Evaluation of Organic–Inorganic Composites. *Nat. Commun.* **2016**, *7* (1), 11811. https://doi.org/10.1038/ncomms11811.

(42) Yang, S.-G.; Xie, H.-J.; Saba, H.; Cseh, L.; Ungar, G. Fluorescence Microscopy Tracking of Dyes, Nanoparticles and Quantum Dots during Growth of Polymer Spherulites. *Polymer* **2020**, *191*, 122246. https://doi.org/10.1016/j.polymer.2020.122246.

(43) Sarkar, A.; Dhiman, S.; Chalishazar, A.; George, S. J. Visualization of Stereoselective Supramolecular Polymers by Chirality-Controlled Energy Transfer. *Angew. Chem. Int. Ed.* **2017**, *56* (44), 13767–13771. https://doi.org/10.1002/anie.201708267.

(44) Giansante, C.; Raffy, G.; Schäfer, C.; Rahma, H.; Kao, M.-T.; Olive, A. G. L.; Del Guerzo, A. White-Light-Emitting Self-Assembled NanoFibers and Their Evidence by Microspectroscopy of Individual Objects. *J. Am. Chem. Soc.* **2011**, *133* (2), 316–325. https://doi.org/10.1021/ja106807u.

(45) de Vet, C.; Gartzia-Rivero, L.; Schäfer, P.; Raffy, G.; Del Guerzo, A. Photocontrolled Hierarchical Self-Assembly of Anisotropic Micropatterns of Nanofibers onto Isotropic Surfaces. *Small* **2020**, *16* (7), 1906723. https://doi.org/10.1002/smll.201906723.

(46) Sethy, R.; Kumar, J.; Métivier, R.; Louis, M.; Nakatani, K.; Mecheri, N. M. T.; Subhakumari, A.; Thomas, K. G.; Kawai, T.; Nakashima, T. Enantioselective Light Harvesting with Perylenediimide Guests on Self-Assembled Chiral Naphthalenediimide Nanofibers. *Angew. Chem. Int. Ed.* **2017**, *56* (47), 15053–15057. https://doi.org/10.1002/anie.201707160.

(47) Sethy, R.; Métivier, R.; Brosseau, A.; Kawai, T.; Nakashima, T. Impact of Optical Purity on the Light Harvesting Property in Supramolecular Nanofibers. *J. Phys. Chem. Lett.* **2018**, *9* (16), 4516–4521. https://doi.org/10.1021/acs.jpclett.8b02015.

(48) Yonezawa, S.; Sethy, R.; Fukuhara, G.; Kawai, T.; Nakashima, T. Pressure-Dependent Guest Binding and Release on a Supramolecular Polymer. *Chem. Commun.* **2019**, *55* (41), 5793–5796. https://doi.org/10.1039/C9CC02696G.

(49) Tsumatori, H.; Nakashima, T.; Kawai, T. Observation of Chiral Aggregate Growth of Perylene Derivative in Opaque Solution by Circularly Polarized Luminescence. *Org. Lett.* **2010**, *12* (10), 2362–2365. https://doi.org/10.1021/ol100701w.

(50) Wong, J. X. H.; Yu, H.-Z. Preparation of Transparent Superhydrophobic Glass Slides: Demonstration of Surface Chemistry Characteristics. *J. Chem. Educ.* **2013**, *90* (9), 1203–1206. https://doi.org/10.1021/ed300809m.

(51) Oyola-Reynoso, S.; Wang, Z.; Chen, J.; Çınar, S.; Chang, B.; Thuo, M. Revisiting the Challenges in Fabricating Uniform Coatings with Polyfunctional Molecules on High Surface Energy Materials. *Coatings* **2015**, *5* (4), 1002–1018. https://doi.org/10.3390/coatings5041002.

(52) Kumar, J.; Tsumatori, H.; Yuasa, J.; Kawai, T.; Nakashima, T. Self-Discriminating Termination of Chiral Supramolecular Polymerization: Tuning the Length of Nanofibers. *Angew. Chem. Int. Ed.* **2015**, *54* (20), 5943–5947. https://doi.org/10.1002/anie.201500292.

(53) Kumar, J.; Nakashima, T.; Tsumatori, H.; Kawai, T. Circularly Polarized Luminescence in Chiral Aggregates: Dependence of Morphology on Luminescence Dissymmetry. *J. Phys. Chem. Lett.* **2014**, *5* (2), 316–321. https://doi.org/10.1021/jz402615n.

(54) Herz, L. M.; Daniel, C.; Silva, C.; Hoeben, F. J. M.; Schenning, A. P. H. J.; Meijer, E. W.; Friend, R. H.; Phillips, R. T. Fast Exciton Diffusion in Chiral Stacks of Conjugated P-Phenylene Vinylene Oligomers. *Phys. Rev. B* **2003**, *68* (4), 045203. https://doi.org/10.1103/PhysRevB.68.045203.

(55) Weston, K. D.; Goldner, L. S. Orientation Imaging and Reorientation Dynamics of Single Dye Molecules. *J. Phys. Chem. B* **2001**, *105* (17), 3453–3462. https://doi.org/10.1021/jp001373p.

(56) Zhang, W.; Jin, W.; Fukushima, T.; Saeki, A.; Seki, S.; Aida, T. Supramolecular Linear Heterojunction Composed of Graphite-Like Semiconducting Nanotubular Segments. *Science* **2011**, *334* (6054), 340–343. https://doi.org/10.1126/science.1210369.

(57) Ha, T.; Laurence, T. A.; Chemla, D. S.; Weiss, S. Polarization Spectroscopy of Single Fluorescent Molecules. *J. Phys. Chem. B* **1999**, *103* (33), 6839–6850. https://doi.org/10.1021/jp990948j.

(58) Mattheyses, A. L.; Hoppe, A. D.; Axelrod, D. Polarized Fluorescence Resonance Energy Transfer Microscopy. *Biophys. J.* **2004**, *87* (4), 2787–2797. https://doi.org/10.1529/biophysj.103.036194.

TABLE OF CONTENT

The self-assembly of a bichromophoric naphthalenediimide (NDI) into nanofibers enables efficient energy transfer to perylenediimide (PDI) molecules through host-guest interactions, as visualized using fluorescence microscopy and AFM. Fluorescence imaging and microspectroscopy revealed packing defects, inhomogeneities, and exciton mobility along the NDI nanofibers, showing strong blue polarized emission from NDI, while PDI guest molecules exhibit minimal polarization.